

**Harnessing bubble behaviors for new analytical strategies**

Journal:	<i>Analyst</i>
Manuscript ID	AN-MRV-07-2020-001497.R1
Article Type:	Minireview
Date Submitted by the Author:	01-Sep-2020
Complete List of Authors:	An, Shizhong; Henan University of Science and Technology, Materials Science and Engineering; Wayne State University Department of Chemistry, Department of Chemistry Ranaweera, Ruchiranga; Wayne State University Department of Chemistry, Department of Chemistry LUO, LONG; Wayne State University Department of Chemistry, Department of Chemistry

ARTICLE

Harnessing bubble behaviors for new analytical strategies

Shizhong An,^{a,b} Ruchiranga Ranaweera^b and Long Luo^{b,*}

Received 00th January 20xx,

Accepted 00th January 20xx

DOI: 10.1039/x0xx00000x

Gas bubbles are easily accessible and offer many unique characteristic properties of a gas/liquid two-phase system for developing analytical methods. In this minireview, we discuss the newly developed analytical strategies that harness the behaviors of bubbles. Recent advancements include the utilization of the gas/liquid interfacial activity of bubbles for detection and preconcentration of surface-active compounds; the employment of the gas phase properties of bubbles for acoustic imaging and detection, microfluidic analysis, electrochemical sensing, and emission spectroscopy; and the application of the mass transport behaviors at the gas/liquid interface in gas sensing, biosensing, and nanofluidics. These studies have demonstrated the versatility of gas bubbles as a platform for developing new analytical strategies.

1. Introduction

Bubbles are not only ubiquitous in our daily life but also are closely related to many industrial processes, such as water electrolysis^{1–5} and Hall–Héroult process.^{6,7} The fundamentals of gas bubble behaviors have been extensively studied, including how they nucleate,^{8–11} grow,^{12–14} interact with other objects,^{15–18} coalesce,^{19,20} detach from a surface or orifice,^{21–24} transport,²⁵ and burst.^{26–29} Recently, there has been an increasing interest in harnessing these well-studied bubble behaviors for new analytical strategies. The motivation is two-fold. First, there are many low-cost and convenient methods for gas bubble generation, such as water electrolysis and directly flowing gas into a liquid medium, which ensures the portability and accessibility of an analytical device. Second, gas bubbles offer many unique features of a gas/liquid two-phase system for developing novel analytical strategies.

In this minireview, we review the most recent works on developing new bubble-based analytical methods. According to their operating principles, we categorize these methods into the following three groups, as illustrated in **Fig. 1**. The analytical methods in the first category take advantage of the gas/liquid interfacial activity of gas bubbles to achieve the detection and preconcentration of surface-active compounds (**Fig. 1a**). In the second category, the gas phase properties of bubbles, such as acoustic resonance, electrical insulation, and electric discharge, were utilized in the analytical method design (**Fig. 1b**). In the

final one, the unusual mass transport behaviors across or along the gas/liquid interface were utilized to attain the desired analytical goals (**Fig. 1c**).

2. Interfacial activity

2.1 Bubble-nucleation-based method for surfactant detection

The gas-liquid interface of gas bubbles has been long exploited for surface tension analysis. Bubble pressure tensiometer, one of the most common tensiometers, is built on the relationship between the internal pressure and surface tension of a gas bubble in the liquid, governed by the Young-Laplace equation.³⁰ Using a bubble pressure tensiometer, one can measure the transient surface tension value that corresponds to the surface tension at a certain surface age. By varying the speed at which bubbles are produced, the dependence of surface tension on surface age or the dynamic surface tension can be measured. Because the dynamic surface tension is a function of the surfactant properties such as concentration, diffusion coefficient, and adsorption coefficient, bubble pressure tensiometer can also be used for the indirect determination of these surfactant properties.³¹

Recently, Ranaweera et al.³² further explored the use of bubbles for surfactant analysis. Unlike the traditional bubble pressure tensiometer, their method is based on electrochemical bubble nucleation. According to the classical nucleation theory, the formation energy of a gas bubble in the liquid is the sum of the energy cost of creating a new gas/liquid interface and the

^a School of Materials Science and Engineering, Henan University of Science and Technology, Luoyang 471023, China

^b Department of Chemistry, Wayne State University, Detroit, Michigan 48202, United States

† Footnotes relating to the title and/or authors should appear here.

Electronic Supplementary Information (ESI) available: [details of any supplementary information available should be included here]. See DOI: 10.1039/x0xx00000x

ARTICLE

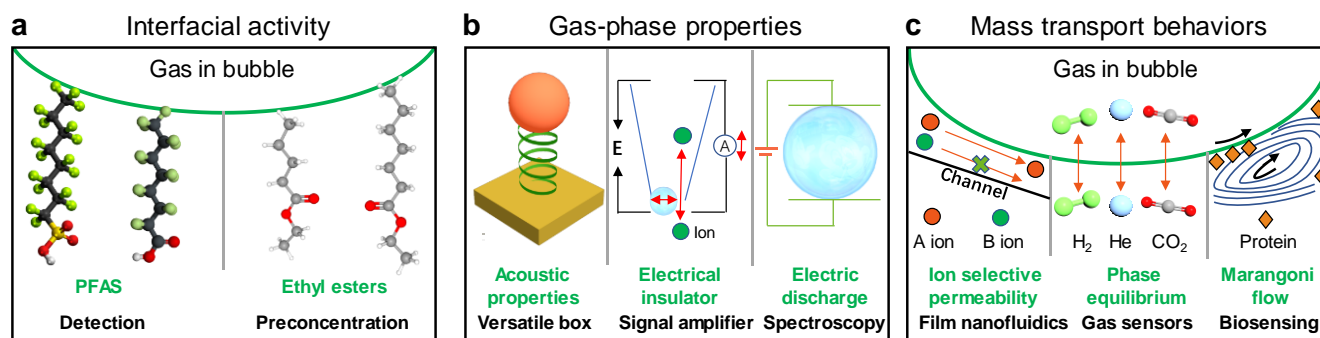


Fig. 1 Three key characteristic properties of gas bubbles that have been utilized for developing new analytical strategies: (a) interfacial activity at the gas/liquid interface; (b) gas-phase properties such as acoustic resonance, electrical insulation, and electric discharge; and (c) unique mass transport behaviors of species at the gas/liquid interface.

energy gain through the liberation of dissolved gas into the bubble volume.^{33, 34} In the presence of surfactants, the surface tension of the gas nucleus/liquid interface decreases, leading to a reduced nucleation energy barrier and accelerated bubble nucleation (**Fig. 2a**). To transduce the bubble nucleation event to an electrochemical signal, they used a nanoelectrode-based approach.^{35–38} In this approach, a single H₂ bubble was generated at a nanodisk electrode by reducing protons electrochemically. The nanoscale dimension of the nanoelectrode is essential to provide the exquisite sensitivity for detecting slight changes near or on the electrode surface (in this case, H₂ bubble nucleation). The peak-shaped voltammograms in **Fig. 2b** are characteristic of the electrochemical nucleation of a single gas nanobubble. The concentration of dissolved H₂ required for bubble nucleation is proportional to the peak current (i_{peak}) in the voltammogram. Because the presence of surfactants facilitates bubble nucleation, i_{peak} decreases with an increasing surfactant concentration. Using this method, they demonstrated the quantitation of perfluorinated surfactants in water, with a remarkable limit of detection (LOD) down to 30 $\mu\text{g/L}$ and a linear dynamic range of over three orders of magnitude (**Fig. 2c**). After preconcentrating the samples for 1000-fold preconcentration using solid-phase extraction, they have achieved a LOD < 70 ng/L (**Fig. 2d**) which is the health advisory for perfluorooctanesulfonate (PFOS) and perfluorooctanoic acid (PFOA) in drinking water established by the U. S. Environmental Protection Agency. They also derived the expression of i_{peak} as a function of the surfactant concentration from the classical nucleation theory and found the theory was in an excellent agreement with the experimental data, confirming the proposed bubble nucleation-based detection mechanism. Because the sensing response originates from the interactions between surfactant molecules and the bubble nucleus, this bubble-nucleation-based method exhibited a superior selectivity towards surfactants (**Fig. 2e** and **f**). It does not respond to inorganic salts, small organic molecules such as humic acids, proteins such as lysozyme, non-surfactant polymers such as poly(ethylene glycol). This method has the potential to be further developed into a universal electrochemical detector for surfactant analysis because of its simplicity and the surface-activity-based detection mechanism.

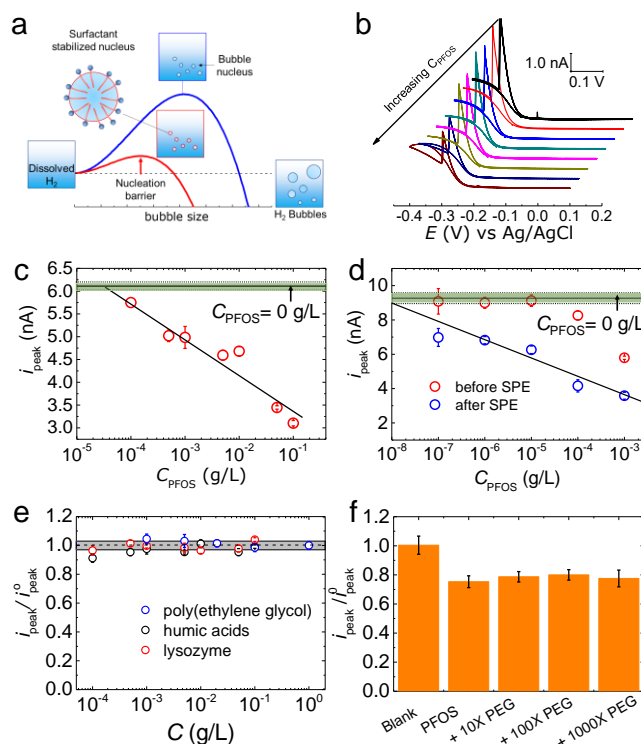


Fig. 2 (a) Schematic diagram illustrating the principle of the bubble-nucleation-based electrochemical method for surfactant detection. (b) Cyclic voltammograms for a Pt nanoelectrode with various perfluorooctanesulfonate (PFOS) concentrations. (c) Plot of i_{peak} vs C_{PFOS} . (d) Plot of i_{peak} vs C_{PFOS} for PFOS samples before and after preconcentration using solid-phase extraction (SPE). (e) Plots of the normalized peak current vs the concentration of poly(ethylene glycol) (PEG), humic acids, and lysozyme. (f) The normalized peak current values for the blank, 10^{-3} g/L PFOS, and 10^{-3} g/L PFOS with 10-, 100-, and 1000-fold excess of PEG. Reprinted with permission from ref. ³², Copyright (2019) American Chemical Society.

2.2 Bubble-bursting-based preconcentration methods

Sea-spray aerosol enrichment is a natural phenomenon.^{39–41} The ocean wind causes a near-surface velocity gradient in the water column that results in wave breaking. The entrainment of air into the water column produces a plume of bubbles. These bubbles

serve to scavenge surface-active materials, carrying them to the air-ocean interface, where the bubbles burst and form a sea-spray aerosol.⁴² These aerosol particles are enriched in surface-active organic materials such as free fatty acids.^{40, 41, 43} The enrichment effect results from the preferential adsorption of surface-active compounds on the bubble surface, creating a high local concentration in the thin layer of solution around the bubble. When these bubbles burst at the liquid/air interface, this thin layer of liquid is ejected to the air and converted to the aerosol droplets containing a high concentration of surface-active compounds.

Chingin et al.⁴⁴⁻⁴⁶ mimicked this natural phenomenon for preconcentration of low-concentration analytes. In their method, gas bubbles were produced in water by flowing gas through an air diffuser. The aerosol droplets formed by bubble bursting were collected. They found the concentration of organic solutes in the collected aerosol droplets increased by 6 to 12-fold for organic metabolites in urine (e.g., lipids and lipid-like molecules, phenylpropanoids and polyketides),⁴⁵ 20 to 1000-fold for rhodamine dyes,⁴⁶ and 10 to 100-fold for amino acids, protein, and DNA.⁴⁴ In most cases, inorganic metal salts were not enriched during the bubble-bursting enrichment of organic solutes. Instead, the inorganic salt concentration notably decreased in the presence of organic components with a relatively high concentration. The proposed desalination mechanism was that inorganic salts and organic compounds were competing for the adsorption sites on the bubble surface. At a high organic solute concentration, metal salts were expelled from the bubble surface by the organic compounds with higher surface activity. They also went one step further to coupling this bubble-bursting-based preconcentration method with mass spectrometry for protein analysis.⁴⁷ More recently, Gao et al.⁴⁸ integrated this preconcentration setup with gas chromatography-mass spectrometry for analyzing trace amounts of dissolved volatiles in complex matrices such as hops, iced coffee, urine, etc.

Inspired by these previous studies, Cao et al.⁴⁹ developed a preconcentration method based on the electrochemical aerosol formation (Fig. 3). Instead of using an air diffuser to produce gas bubbles, they *in situ* generated H₂ microbubbles by electrochemically reducing water. Electrogeneration of bubbles has the following benefits: (1) it provides precise control of the bubble flux by adjustment of the current through the electrodes; (2) it minimizes the initial momentum of gas bubbles, which helps to achieve a predictable low Reynolds number motion of bubbles;⁵⁰⁻⁵² and (3) it reduces random bubble coalescence, which often occurs when flowing gas through a porous frit to generate bubbles.²⁷ They applied this method to the preconcentration of per- and polyfluorinated alkyl substances (PFAS), a group of emerging surfactant contaminants in the environment that has a very low LOD of interest (<70 ng/L). This method exhibited a constant 1000-fold preconcentration of PFOS within 10 minutes in the concentration range of 0.5 ng/L to 500 ng/L (Fig. 3b). A similar enrichment factor, *R*, of ~1000 was achieved for ten common PFAS (Fig. 3c), including seven perfluorinated carboxylic acids with a carbon chain length from 6 to 12 (PFHxA, PFHpA, PFOA, PFNA, PFDA, PFUnDA, and PFDoDA) and three perfluorinated sulfonic acids (PFBS, PFHxS, and PFOS).

and PFOS). Impressively, the *R*-value varied by < 10% over a concentration range from 10⁻¹² to 10⁻⁹ M for all tested PFAS analytes. They further tested the simultaneous preconcentration of multiple PFAS analyte in a tap water sample. They observed that the enrichment factor for each analyte was consistent with the predetermined values using the individual standard solutions (Fig. 3d). Their mechanistic study revealed that the diffusion-controlled adsorption of PFAS to the bubble surface determined the enrichment efficiency of this method (Fig. 3e). In comparison to solid phase extraction, the standard preconcentration method in PFAS analysis, this new method is much simpler (one step vs multistep), quicker (10 min vs up to several hours), and free of organic solvent.

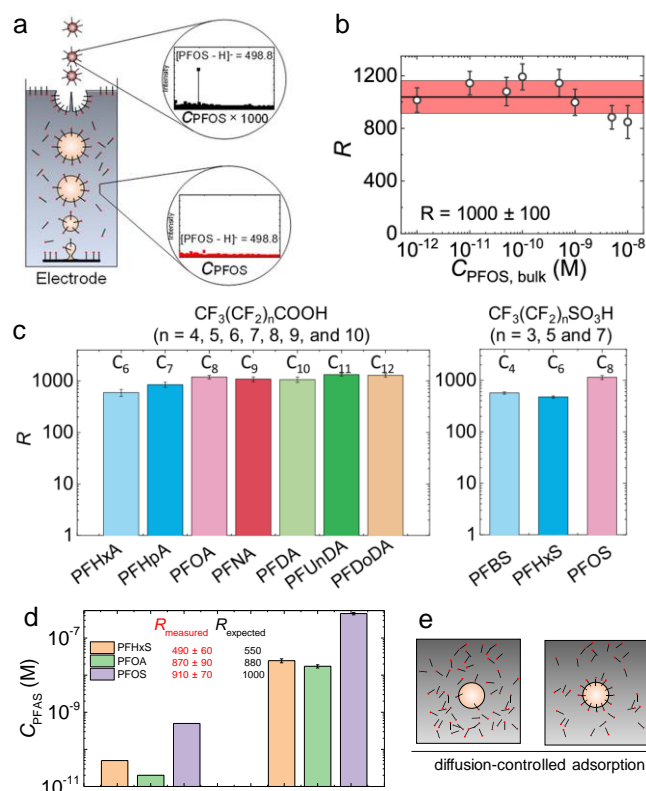


Fig. 3 (a) Schematic diagram illustrating the principle of preconcentration of per- and polyfluorinated alkyl substances (PFAS) via electrochemical aerosol enrichment. (b) Dependence of enrichment factor, *R*, on the PFOS concentration in the bulk solution (C_{PFOS, bulk}). *R* is defined as the ratio of PFOS concentrations in the aerosol (C_{PFOS, aerosol}) and its corresponding C_{PFOS, bulk}. (c) *R* for ten common PFAS at C_{PFOS, bulk} = 10⁻¹⁰ M. (d) PFAS concentrations before and after preconcentration. The measured preconcentration factor, *R*_{measured}, vs the expected preconcentration factor, *R*_{expected}, for each PFAS compound spiked in the tap water sample. The *R*_{expected} values are the *R* values for each PFAS compound obtained using the standard solutions. (e) The enrichment efficiency is dictated by the diffusion-limited adsorption of PFAS to the bubble surface. Reprinted with permission from ref. ⁴⁹, Copyright (2019) American Chemical Society.

In addition to the two bubble-generation approaches discussed above, gas bubbles can also be produced in liquid for preconcentration by sudden decompression of a solution originally supersaturated with gas,⁵³⁻⁵⁶ by microfluidic approaches,⁵⁷ or by *in situ* chemical reaction⁵⁸. Fig. 4a shows the experimental setup developed by Elpa et al.⁵⁸ for rapid extraction and analysis of volatile solutes with an effervescent tablet. The

tablet comprises of NaHCO_3 and NaH_2PO_4 , which react and generate CO_2 gas upon contact with an aqueous sample (Fig. 4b). The composition of headspace gas was analyzed by atmospheric pressure chemical ionization (APCI)-mass spectrometer (MS) (Fig. 4a). Using seven ethyl esters as model analytes, they showed that the APCI-MS signals of these analytes dramatically increased after initiating the bubble generation reaction of one tablet (Fig. 4c). This method is compatible with gas chromatography-mass spectrometry and headspace-solid phase microextraction. It is worth noting that this method transfers volatile/semivolatile compounds (VOCs) from liquid matrices directly to the gas phase, and not to aerosol droplets as others' work. They proposed two possible transfer pathways: (1) VOCs were released from the aerosols over the liquid surface during aerosol evaporation; and (2) VOCs in the solution were transferred to bubble lumens and then liberated directly to the headspace when bubbles burst.

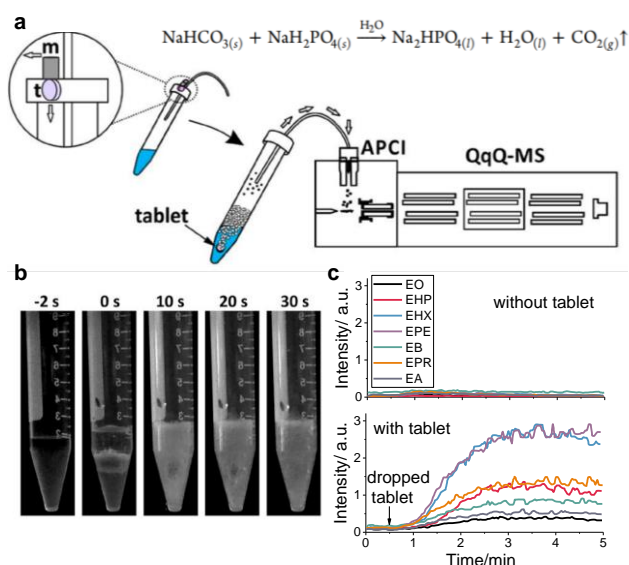


Fig. 4. (a) The experimental setup that integrates effervescent tablet-induced extraction with atmospheric pressure chemical ionization (APCI)-mass spectrometer (MS). (b) NaHCO_3 and NaH_2PO_4 in the tablet react to generate CO_2 gas bubbles upon contact with an aqueous sample. (c) APCI-MS signal intensities for seven different ethyl esters without a tablet (top) and with one tablet added to the analyte solution. Reprinted with permission from ref. ⁵⁸, Copyright (2020) American Chemical Society.

3. Gas-phase properties

3.1 Acoustic properties: A versatile toolbox

Bubbles are compressible gas-filled entities. In an acoustic field, they compress and expand at the pressure peaks and nadirs, respectively.⁵⁹ Contrast-enhanced ultrasound imaging (CEUS), a widely-used non-invasive diagnostic test, is one most well-known application of the acoustic properties of gas bubbles.⁶⁰⁻⁶⁴ Ultrasound imaging relies on the reception, analysis, and display of acoustic signals produced by reflection or backscatter of ultrasound from internal organs. Because microbubbles undergo radial oscillation upon ultrasound excitation, they generate strong acoustic signals, greatly exceeding conventional ultrasound backscatter produced by reflection or alteration in acoustic impedance. As an example, Fig. 5a and b show the

images of a patient's gallbladder using conventional ultrasound (US) and CEUS with phospholipid-stabilized microbubbles filled with SF_6 gas.⁶⁵ The CEUS provides better contrast than the conventional US, which is critical for differentiating between benign and malignant polypoid lesions of the gallbladder. Microbubble-based CEUS is also adopted in the diagnostic imaging of other organs including liver, kidney, pancreas, spleen, etc.⁶⁶ Because microbubbles vibrate at a characteristic eigenfrequency which is inversely proportional to their size, the size control of microbubbles is critical to improve the ultrasonic imaging contrast. Compared to conventional CEUS which usually generates microbubbles within a large range of size, microfluidic device is a good choice to produce monodisperse microbubbles for better imaging. Segers et al.⁶⁹ showed that monodisperse suspensions (1-5 μm) of lipid-coated microbubbles could be microfluidically formed at clinically relevant concentrations and at a yield of 100% by filling the freshly formed bubbles with a precisely tuned gas mixture of a high- and a low-aqueous solubility gas. Besides, antibubble, which is a gas bubble containing a liquid droplet core, generates stronger harmonic signal component than identical bubbles without a core, showing that the antibubbles are candidates for harmonic imaging.⁷⁰

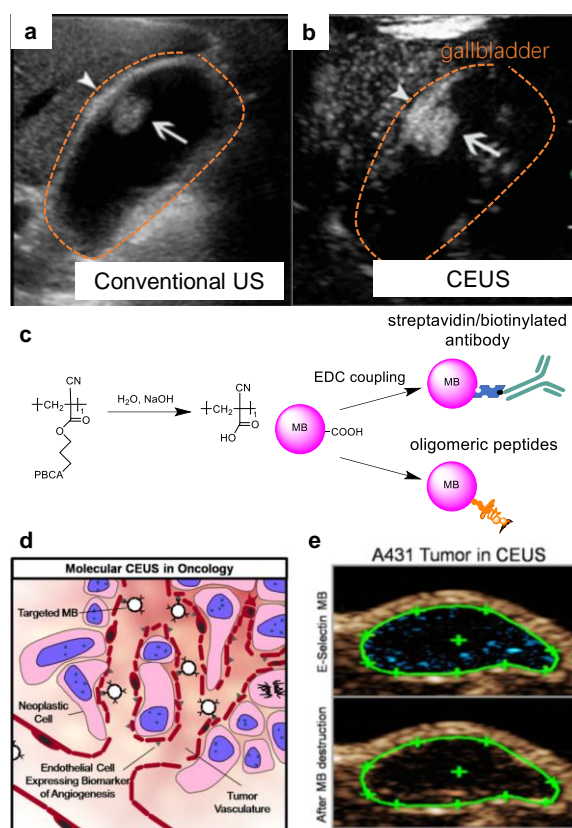


Fig. 5. (a) and (b) Images of a patient's gallbladder using conventional ultrasound (US) and contrast-enhanced ultrasound (CEUS), respectively. CEUS used phospholipid-stabilized microbubbles (MBs) filled with SF_6 gas to improve the image contrast for more accurate differentiation between benign and malignant polypoid lesions. (c) Synthesis and functionalization of MBs with poly(n-butyl cyanoacrylate) (PBCA) shell for targeted CEUS. (d) Illustration of the binding of MBs to endothelial cells that express angiogenesis biomarkers during tumor progression for CEUS imaging. (e) Targeted CEUS images of a

subcutaneous A431 xenograft tumor. Reprinted with permission from ref. ⁶⁵, Copyright (2013) IOS Press and from ref. ⁶⁷, Copyright (2017) Elsevier.

Recent technology development of the CEUS has been focused on targeted CEUS, where microbubbles modified with biorecognition elements such as peptides and antibodies are used to achieve targeted imaging and therapy.⁶⁸ For example, **Fig. 5c** shows the synthesis and functionalization of microbubbles with poly(*n*-butyl cyanoacrylate) (PBCA) shell.⁶⁷ After partial hydrolysis of the PBCA shell, carboxylate functional groups are exposed, allowing the direct EDC coupling with the streptavidin/biotinylated antibody conjugates or small oligomeric peptides (EDC stands for N-(3-dimethylaminopropyl)-N-ethylcarbodiimide hydrochloride). **Fig. 5d** illustrates the binding of microbubbles to endothelial cells that express angiogenesis biomarkers during tumor progression for CEUS imaging. **Fig. 5e** shows the CEUS images of a subcutaneous A431 xenograft tumor. The peptide modified microbubbles recognize E-selection, a glycoprotein expressed on tumor blood vessels.

Besides the medical use in ultrasound imaging, gas bubbles are also employed for acoustic detection, blocking, focusing, and imaging.^{71–74} For example, Cai et al.⁷⁵ developed a bubble-based acoustic detector which has a three-dimensionally printed hydrophobic hollow frame structure. When the device was immersed underwater, one gas bubble was trapped in each cubic frame of the device. The trapped bubble and the water layer above the bubble form a mass-spring system, in which the bubble is a spring and the water layer is the mass. When a sound wave propagates through this mass-spring system, the transmission of a sound wave is at the maximum if the sound frequency matches its resonant frequency; otherwise, the sound wave gets significantly reflected at the gas/liquid interface, leading to a low sound level above the liquid surface. Because the resonant frequency depends on the gas bubble dimension and the mass of the water layer above the bubble, the selective detection of a particular frequency was achieved by simply placing the device at different immersion depths. The same group also designed new patterns of gas bubble arrays for acoustic blocking.⁷⁶ In their design, a cover plate and a hydrophobic pillar-structured substrate sandwiched a single layer of gas bubbles. When an ultrasonic wave passes through the device, this bubble layer acts as a nearly perfect mirror, reflecting the sound wave at the low frequencies and reducing the transmission of the low-frequency ultrasonic waves. At a sound frequency close to the resonant frequency of the bubbles, the transmission magnitude reaches the minimum due to the Minnaert resonance effect.⁷¹ By adjusting the bubble array pattern, the operating frequency was tunable in the range from 9 to 1756 kHz, with only less than 0.2% of the sound energy transmitted. Note that acoustic enhancement and blocking discussed above happen at different sound frequencies and have different physical origins. The enhanced transmission results from the Fabry–Perot resonance, where the thin water layer above the bubbles is essential in the resonance, whereas the transmission blockage is due to the Minnaert resonance effect.⁷¹

Microfluidics is another field that frequently uses the acoustic properties of gas bubbles. Microfluidic devices manipulate a minimal amount of fluids. Introduction of a new

phase like gas bubbles to the fluids leads to multiphase flows, which significantly expands the functionality of a microfluidic device.^{77–80} In a recent review, Hashmi et al.⁸¹ summarized the lab-on-a-chip applications of oscillating microbubbles in literature before 2012. Briefly, gas bubbles were used as a pump to drive directional flows in microchannels, as a micro-mixer to achieve fast mixing, as a filter to sort particles, and as a transporter to move samples from one location to another. The application scope has continued expanding in recent years.^{82–86} **Fig. 6a** shows the acoustic microfluidic device developed by Ahmed et al.⁸³ for precise rotational manipulation of single cells and organisms. The piezoelectric transducer generates acoustic waves to actuate air microbubbles trapped within sidewall microcavities in a microfluidic channel. The oscillating microbubbles establish an intricate microstreaming pattern. In the *x*-*y* plane, the liquid flow pattern is characterized by two symmetric vortices in the plane of oscillation (**Fig. 6b**). Along the *x*-axis, single out-of-plane microstreaming vortex exists as a result of microbubble shape distortion that occurs due to the difference in contact angles between the glass substrate and the channel ceiling (**Fig. 6c**). This out-of-plane vortex enables a delicate control of the rotational motion of single cells, such as HeLa cells and organisms such as the *C. elegans* worm in **Fig. 6d**. This bubble-based single entity manipulation tool is valuable in the fields of bioengineering, biophysics, medicine, and developmental biology.

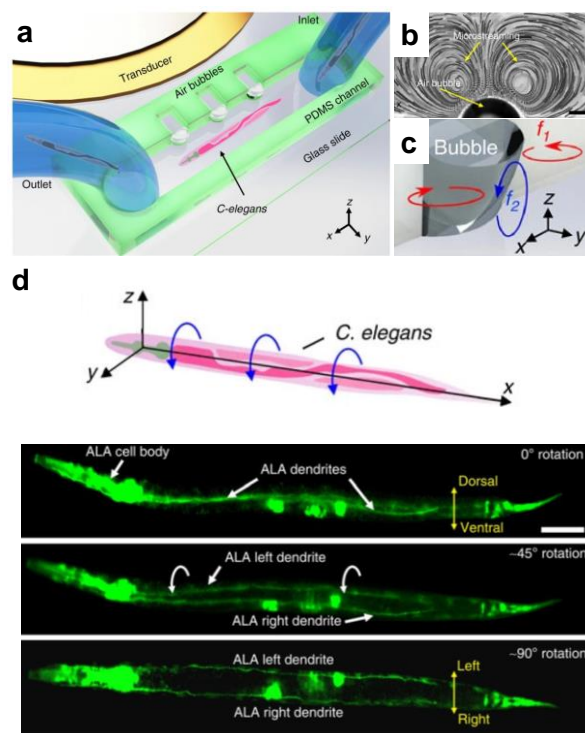


Fig. 6. (a) Schematic of the experimental setup for rotational manipulation of single cells and organisms using acoustic microstreaming induced by oscillating microbubbles. (b) An optical image of acoustic microstreaming in the *x*-*y* plane during microbubble oscillation. (c) 3D sketch demonstrating in-plane (red) and out-of-plane (blue) acoustic microstreaming vortices around a microbubble. (d) The rotational motion of *C. elegans* caused by the simultaneous oscillation of multiple microbubbles and its fluorescence image at different rotation angles. Reprinted with permission from ref. ⁸³, Copyright (2016) Springer Nature Limited.

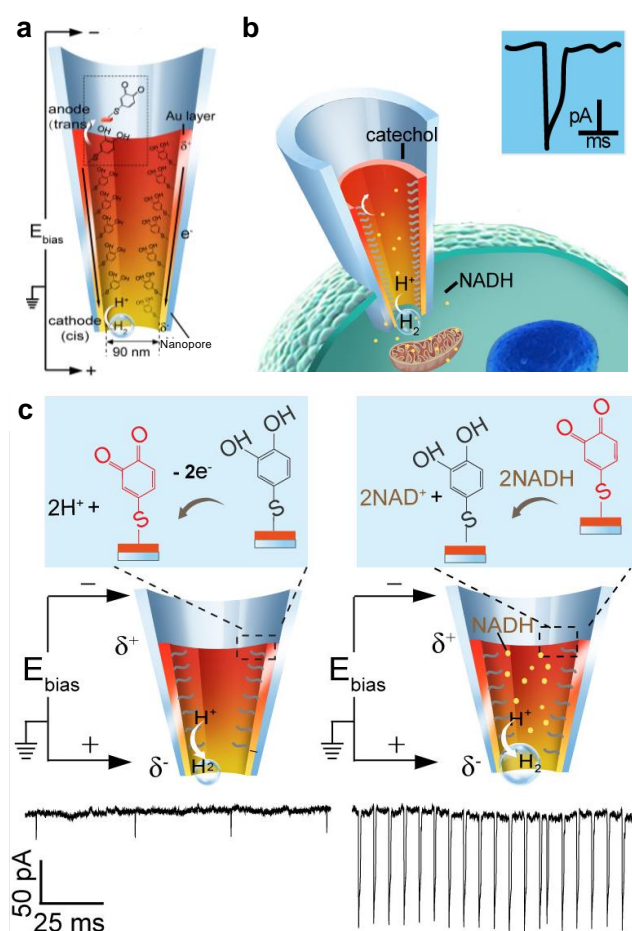


Fig. 7. (a) and (b) The design of a nanobubble-based signal amplifier for probing redox-active species in living cells. A voltage bias (E_{bias}) was applied between the two terminals of an Au-coated nanopipette, driving different redox reactions at the two ends of the Au film. Electrooxidation of the target analyte, nicotinamide adenine nucleotide (NADH), took place at the *trans* end of the Au film and the reduction of water to H_2 at the *cis* end. The water reduction reaction led to H_2 bubble formation, blocking the ionic flow in the nanopipette and generating a current transient. The catechol on the Au film catalyzes the electrooxidation of NADH. (c) Current-time traces in the absence and presence of NADH. Because the oxidation of NADH and bubble formation are coupled following a bipolar electrochemistry mechanism, the presence of NADH led to a significant bubble formation and, thus, a large electrical signal. Reprinted with permission from ref. ⁸⁷, Copyright (2018) American Chemical Society.

3.2 Electrical insulator: A nanoscale signal amplifier

Gas bubbles are electrically insulating under ambient conditions. Ying et al.⁸⁷ devised an innovative electrochemical signal amplifier using this property for probing redox-active species in living cells. In their design, they coupled electrochemical H_2 nanobubble formation with electrocatalytic oxidation of a target analyte, nicotinamide adenine nucleotide (NADH), via bipolar electrochemistry. The bipolar electrode was a thin Au film on the interior wall of a nanopipette (Fig. 7a). The small dimension of the nanopipette is essential for performing the analysis of single cells (Fig. 7b). When a voltage bias is applied between the two terminals of the nanopipette, the Au film is polarized by the electric field, driving the NADH oxidation at one end of the Au film and the water reduction to H_2 at the other. The two reactions co-occur at an identical rate. Because the amount of NADH release in a cell is minimal, it has been challenging to monitor the NADH release by directly measuring the faradaic current of NADH

oxidation. However, after coupling the NADH oxidation with water reduction to H_2 , this low current is transduced to bubble formation, which blocks the ionic transport in the nanopipette and dramatically amplifies the electrical signal. Fig. 7c shows the current-time traces in the absence and presence of NADH. Note that the Au film was modified with catechol, a catalyst that facilitates the electrooxidation of NADH. They demonstrated that this signal amplification method enabled highly selective and sensitive probing of NADH concentrations as low as 1 pM. The most exciting feature of this method is that it can be applied to the characterization of many different redox-active species in living cells by modifying the gold film with the corresponding redox probes. Therefore, it holds great potential in analyzing critical bodily processes in multicellular and unicellular organisms

3.3 Electric discharge: Optical emission spectroscopy

Electric discharge in the gas phase has been extensively studied and used in industry for over 100 years. In comparison, plasma in or in contact with water is a relatively new field, which has been growing fast in recent years.⁸⁸ Electric discharge of gas bubbles in water requires a considerably higher electric field than that of atmospheric gas because the concentration of water vapor is approximately 1000 times higher than that of atmospheric gas.⁸⁹ During the electric discharge of gas bubbles in water, high-energy radicals, ions, and molecular species are produced, making it well-suited for applications like water treatment.⁹⁰ Meanwhile, the optical emissions associated with these high energy particles has led to the development of new analytical methods for elemental analysis. For example, Kohara et al.⁹¹ developed the liquid electrode plasma atomic emission spectrometry. In their setup, they fabricated an hourglass microchannel (Fig. 8). When a high-voltage pulse (800 to 2500 V) was applied between the two ends of the microchannel, a gas bubble was generated by Joule heating at the narrow-center part. When the bubble expanded, it blocked the channel, establishing a strong electric field inside the bubble to trigger the electric discharge as well as atomic emission. Fig. 8 shows the images of the atomic emission in the device for solutions containing different metal ions. Using the atomic emission signal, they demonstrated the detection of 41 elements and the limits of detection comparable to the flame atomic absorption spectrometry. Do et al.⁹² and Barua et al.⁹³ further extended this method to the determination of total cesium in radioactive liquid waste and on-site analysis of gold, palladium, and platinum in metallurgical waste leachates after necessary modifications of the experimental setup. The electric discharge of gas bubbles is not only useful for metal analysis but can also be a potentially powerful tool for gas identification. Hamdan et al.⁹⁴ studied the nanosecond electric discharge in water bubbled with different gases, such as argon, methane, carbon dioxide, and propane. In their experimental setup, they aligned a pin electrode and a hollow needle electrode, flew gas through the lower hollow needle to form bubbles between the two electrodes, and discharged the bubbles by applying a nanosecond high-voltage (up to 15 kV) pulse. They observed emission spectra with different signature peaks for gas bubbles with different gas types, which can be used for the identification of gas compositions.

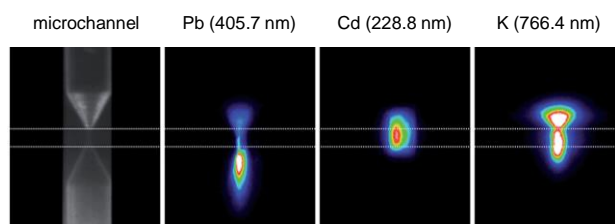


Fig. 8. Images of the hourglass shape microchannel used in the liquid electrode plasma atomic emission spectrometry for elemental analysis, and the atomic emissions in the channel for solutions containing different metal ions. Reprinted with permission from ref. ⁹¹, Copyright (2015) Royal Society of Chemistry.

3.4 Deformability: Bubble-in-drop microextraction

Single droplet microextraction is a microscale variation of liquid–liquid extraction,^{95, 96} where a droplet of the extraction solvent is suspended at the tip of the needle of a microsyringe and immersed in the gaseous or liquid sample for extraction. After extraction, the solvent droplet is withdrawn back into the microsyringe and then injected into an instrument for analysis. Single droplet microextraction is known for its high extraction efficiency and simplicity of operation. Williams et al.⁹⁷ further improved the extraction efficiency of single droplet microextraction by deliberately introducing a certain volume of air into the droplet to increase its surface area. This modified microextraction method was named as the bubble-in-drop microextraction. They showed this simple change improved the extraction efficiency for ten different triazine compounds by 2- to 3-fold as compared with traditional single droplet microextraction. The same group later applied the bubble-in-drop microextraction method to the rapid detection of atrazine and metolachlor, two common herbicides in farm soils.⁹⁸ Lee and coworkers automated this extraction method, coupled it with gas chromatography/mass spectrometry, and applied to the analysis of nitro musks,⁹⁹ organochlorine pesticides,¹⁰⁰ and carbamate pesticides¹⁰¹ in environmental water samples. They evaluated the effects of various parameters on the extraction efficiency, including the type of extraction solvent, the volume of the air bubble, extraction temperature, extraction time, and effect of salt addition. At the same time, George et al. applied the bubble-in-drop microextraction to the analysis of phthalic acid esters in soil samples,¹⁰² and quantification of growth hormones in bovine urine.¹⁰³

4. Mass transport behaviors

4.1 Gas transport across the gas/liquid interface

Once a gas bubble is generated in a liquid medium, it begins to shrink as a result of the gas diffusion across the gas/liquid interface into the liquid phase. According to the Epstein-Plesset equation,¹⁰⁴ the bubble size change is mainly controlled by three gas-identity-dependent parameters: gas diffusivity, gas solubility in the liquid normalized by density, and the ratio of initial dissolved gas concentration to the saturation dissolved gas concentration. Based on this relationship, Bulbul et al.¹⁰⁵ devised a bubble-based microfluidic gas sensor that could identify and quantify gases for gas chromatography (**Fig. 9a**). In their design,

a gas mixture first passes through a gas chromatography column to be separated as individual components. The gas flow then enters a microfluidic channel to form gas bubbles. Because the bubble size is a function of the gas identity and composition, by monitoring the size change of bubbles, the device generates a chromatogram that contains the identity and composition information of the gas sample. To test the feasibility of this concept, they first studied gas bubble formation in a microfluidic channel.¹⁰⁶ They found that different gases required different characteristic gas pressure and flow rate to form gas bubbles, and the resulting bubble volume in the microfluidic channel was dependent on the gas identity (**Fig. 9b**). Most interestingly, they discovered a nearly linear relationship between the bubble size and the composition of a gas mixture (**Fig. 9c**). For a CO₂/N₂ mixture, the higher CO₂ concentration is, the smaller the gas bubbles are. These initial findings have confirmed the feasibility of identifying and quantifying a gas sample by analyzing its bubble behavior in a microfluidic channel. Further, they demonstrated the identification of a pulse of pentane gas in a continuous flow of helium gas by optically tracking the gas bubble size change as a function of time (**Fig. 9d**).¹⁰⁵ They next tested the quantification capability of their sensor.¹⁰⁷ They estimated the injected volume of a gas analyte from the total volume of gas bubbles and found the results were in excellent agreement with the ones determined by commercial gas chromatography with a flame-ionization detector. Most recently, they established a theoretical model for this sensing method.¹⁰⁸ Their model describes the gas loss due to mass transfer from the bubble to the liquid medium during bubble formation in a microfluidic device. The volume loss of bubbles under various conditions derived by this model was well-matched with the experimental value.

The bubble shrinkage phenomenon in a microfluidic channel was also adopted by Seo et al.¹⁰⁹⁻¹¹¹ to evaluate the performance of their carbon sequestration method. In their method, engineered nanoparticles, such as Ni nanoparticles, were employed as the CO₂-to-HCO₃⁻ conversion catalyst, which accelerates the solubility trapping and mineralization of CO₂ from the gas phase into a saline aquifer.¹¹⁰ To quantify the catalytic activity of these nanoparticles, they generated uniform CO₂ microbubbles in a microfluidic channel filled with a nanoparticle solution. Because the CO₂-to-HCO₃⁻ conversion affects the dissolved CO₂ concentration near a CO₂ bubble, which changes the shrinkage rate of gas bubbles, the catalytic activity of nanoparticles can be evaluated from the bubble shrinkage rate.

Unlike gas bubbles in the liquid, soap bubbles have two gas/liquid interfaces stabilized by surfactant molecules, forming a liquid thin film with a high surface area to volume ratio. When gas molecules diffuse across these two interfaces, this liquid film samples them. Kanyanee et al.¹¹² developed an SO₂ gas sensor using this property of soap bubbles. In their sensor, they incorporated H₂O₂ into a soap bubble. In the presence of low concentrations of SO₂ gas, H₂O₂ in the bubble film reacts with SO₂ to form an ionic species, SO₄²⁻, leading to an increased electrical conductance of the bubble film. This unique soap bubble gas sensor was capable of detecting sub-ppm levels of

SO₂. They further modified the soap bubble system by introducing α -cyclodextrin to the bubble film.¹¹³ Because α -cyclodextrin selectively binds with α (+)pinene, the α -cyclodextrin-doped bubble film enabled the selective transport of α (+)pinene in a mixture of α (\pm)pinene. More recently, Fu et al.¹¹⁴ followed up on Kanyanee's initial work and reported a Newton black film for selective formaldehyde gas detection. Newton black film designates a special equilibrium state of a soap film, where the film thickness is less than 7 nm and is not sensitive to the changes of the liquid composition such as ionic strength. The selective detection of formaldehyde was achieved by the Hantzsch reaction between formaldehyde, acetylacetone, and ammonium citrate to form 3,5-diacetyl-1,4-dihydrolutidine, a highly fluorescent species for quantification. This method exhibited a limit of detection of 4 ppb, a linear sensing range up to 300 ppb, and high selectivity for formaldehyde over other interfering aldehydes. Using a similar design, they developed a gas sensor for NH₃ and acetic acid gas detection by incorporating a pH-sensitive fluorescent dye into the soap film to produce the fluorescence signal.¹¹⁵

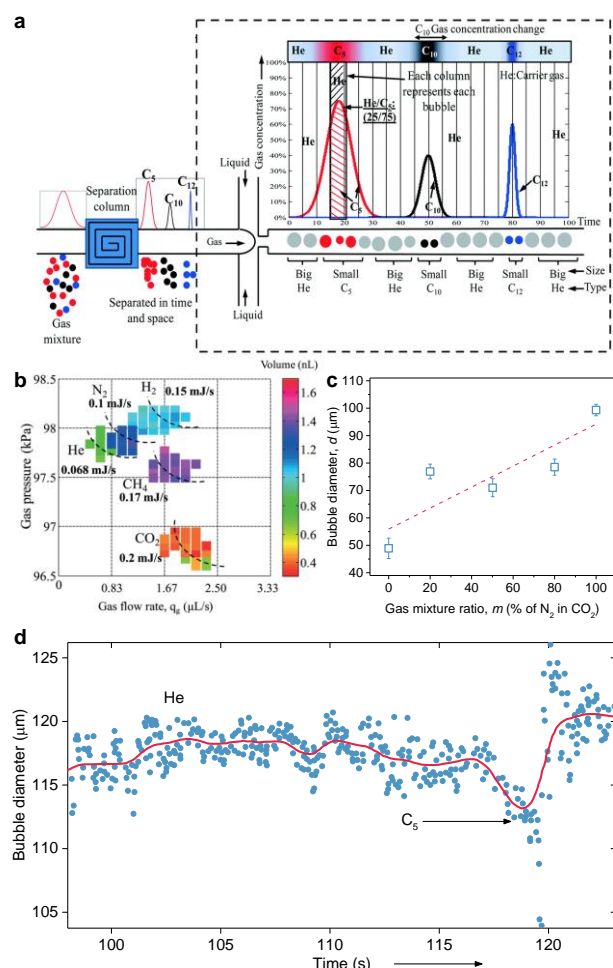


Fig. 9. (a) The concept of bubble-based gas sensing for gas chromatography. A column first separates individual components in a gas mixture, which then enters a microfluidic device (the dashed rectangular region) to form a train of gas microbubbles. Because the size and number of gas bubbles are a function of the identity and quantity of each gas component, a chromatogram is generated by optically tracking the sizes of these bubbles. (b) The volume of gas bubbles generated in the microfluidic device as a function of gas

pressure and gas flow rate for different gas types. (c) Bubble diameter vs the gas composition in a CO₂/N₂ mixture. (d) Bubble size variation for one pentane (C₅) injection in a continuous He flow. Bubbles sharply reduce their diameters when the device experiences a transition from He gas to C₅ gas at ~120 s. Reprinted with permission from ref.¹⁰⁵, Copyright (2015) Royal Society of Chemistry.

4.2 Ion transport along the gas/liquid interface

In the previous section, we discussed the transport phenomena across the gas/liquid interface of gas bubbles or soap bubbles. The transport phenomena along the gas/liquid interface are equally exciting. In this transport mode, the surface charge on the gas/liquid interface plays an essential role. The Bianco group has pioneered in the research on the electrokinetic properties of soap bubble films with nanometric thickness.¹¹⁶⁻¹¹⁸ They discovered that the conductance of a nanometer-thick soap film was independent of the film thickness and was no longer a linear function of electrolyte concentration, indicating that the ion transport in the film deviates from its bulk properties. This deviation is caused by the surface conductivity becoming dominant over the bulk one as the film thickness enters the nanoscale regime. The ionic surfactants at the gas/liquid interface strongly affect the surface conductivity by interacting with the mobile ions near the interface via electrostatic interactions. Similar surface effects have also been reported in studies on ion transport in solid-state nanochannels or nanopores.^{119, 120} However, unlike solid-state nanochannels or nanopores, soap films are not rigid. As a result, ion transport in the soap film is often accompanied by the deformation of the film due to a surface charge-induced electroosmotic flow.¹¹⁶

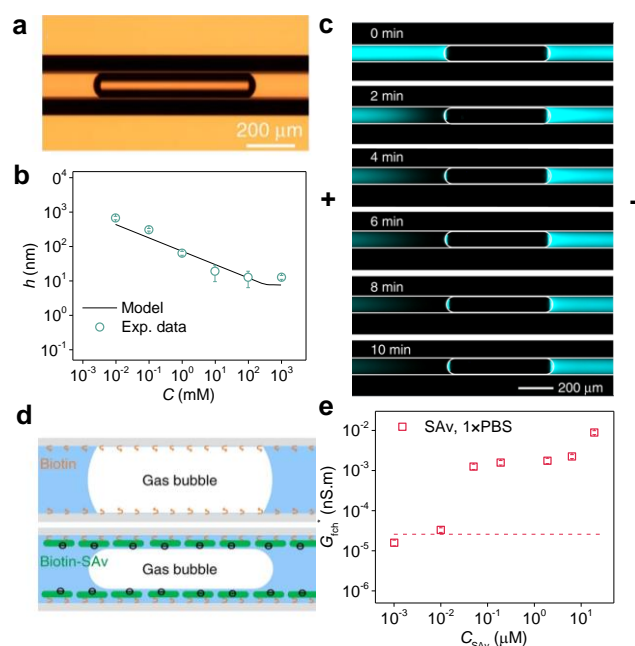


Fig. 10. (a) A photograph of a bubble film nanochannel prepared by inserting a gas bubble in a capillary. (b) The film nanochannel thickness, h , as a function of salt concentration, C . (c) Ion concentration polarization phenomenon caused by the ion permselectivity of the bubble film nanochannel. Fluorescein, an ionic fluorescent tracer, was depleted from the left side of a gas bubble in the capillary when a voltage bias was applied in the capillary. (d) Schematics illustrating the principle of sensing the biotin-streptavidin (SAV) binding. (e) The film nanochannel conductance normalized the bubble length, G_{ich}^* , as a function of SAV concentration in the phosphate-buffered saline (PBS). Reprinted with permission from ref.¹²¹, Copyright (2020) Springer Nature Limited.

Based on these prior findings, Ma et al.¹²¹ developed a bubble film nanochannel for biomolecule sensing. In their design, a gas bubble was inserted in a glass capillary filled with a salt solution (Fig. 10a), forming a liquid film channel between the gas bubble and glass capillary, which structurally resembles a soap film. The thickness of the liquid film can be varied from 10 nm to sub-micrometer by adjusting salt concentration or pH (Fig. 10b). The film nanochannel exhibits ion permselectivity because the charge carriers in the film are predominantly cations attracted by the negatively charged bubble surface and capillary wall. The selective passing of the cations through the film nanochannel led to ion concentration polarization (ICP). ICP is an electrokinetic phenomenon where the accumulation of charged species occurs in one compartment (ion enrichment) and ion depletion in the other.¹²²⁻¹²⁴ Fig. 10c shows the depletion of fluorescein, an ionic fluorescent tracer, on the left side of the film nanochannel after applying a voltage bias in the capillary. ICP occurs because cation permselectivity caused a depletion of cations and accumulation of anions on the left side of the trapped bubble. However, the accumulation of anions alone is not favorable because of electrostatic repulsion between anions, eventually resulting in an ion depletion zone in the channel, as evidenced by the disappearance of fluorescence in Fig. 10c. Because the conductance of the film nanochannel is highly sensitive to the surface charge on the capillary wall, they built a sensor that responds to the biochemical binding reaction on the surface, such as biotin-avidin binding (Fig. 10d). Fig. 10e shows the normalized film nanochannel conductance as a function of streptavidin concentration for a biotin-modified capillary. This bubble-based method provides easy access to the unique ion transport behaviors at the nanoscale, opening many possibilities for analytical applications.

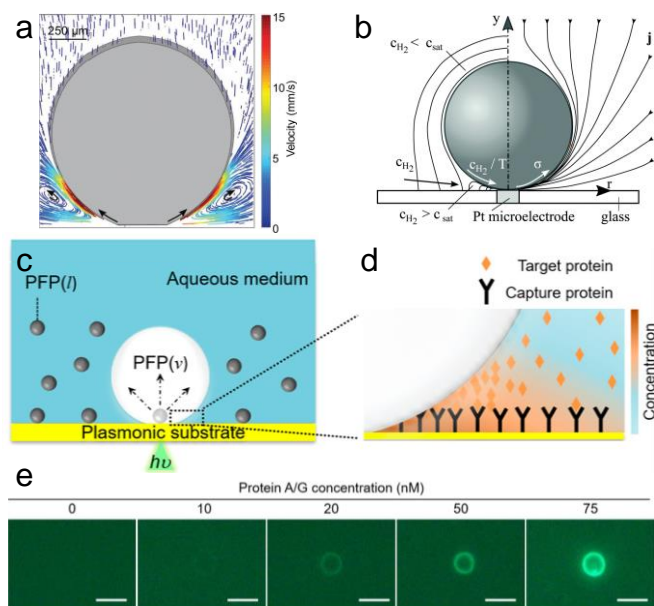


Fig. 11. (a) Flow velocity around an electrogenerated H_2 bubble measured by particle tracking velocimetry indicating the existence of Marangoni convection near this electrogenerated bubble. (b) Schematic distribution of the current density (j) and the hydrogen concentration (C_{H_2}) around the electrogenerated gas bubble. The high local C_{H_2} and temperature (T) at the bottom of the gas bubble resulted in a gradient of surface

tension, σ , at the gas/liquid interface, leading to the formation of Marangoni flow. (c) Schematic illustration of the opto-thermal bubble-generation in a perfluoropentane (C_5F_{12} , PFP)-in-water system and (d) concentration of target proteins near the bubble-liquid-substrate interface due to the presence of Marangoni flow around the PFP vapor bubble. (e) Fluorescence images of substrates after the bubble concentration of fluorescent protein A/G at varying concentrations. Reproduced with permission from ref. ¹²⁵, copyright (2018) by the Royal Society of Chemistry, and from ref. ¹²⁶, copyright (2020) by American Chemical Society

4.2 Marangoni flow around a gas bubble

The Marangoni effect describes the movement in a fluid interface caused by local variations of interfacial tension that are caused in turn by the difference in composition or temperature.¹²⁷ Marangoni flows are present around electrochemically and thermally generated gas bubbles.^{125, 128, 129} Fig. 11a shows the Marangoni flow velocity field around an electrogenerated H_2 bubble sitting on a platinum microelectrode measured by particle tracking velocimetry.¹²⁵ The formation of the gas bubble displaces the electrolyte near the electrode surface. The increased ohmic loss leads to significant heating of the electrolyte, especially near the microelectrode, where the current density is at its maximum. Meanwhile, the concentration of dissolved H_2 is also at the maximum near the microelectrode. The distribution of temperature and dissolved H_2 concentration establishes a surface tension gradient at the gas/liquid interface (Fig. 11b), driving a high-velocity convective flow in the electrolyte and the gas bubble (Marangoni effect). The characteristic vortex flows around the gas bubble drags species from the bulk solution to the gas bubble. Taking advantage of this behavior, Zheng and coworkers developed bubble-pen lithography,¹³⁰⁻¹³² where they opto-thermally generated Marangoni convection around a vapor bubble to bring objects from the bulk solution to the bubble and trap them there. Most recently, they modified this patterning method and applied it to enhance surface capture and sensing of proteins.¹²⁶ In the modified setup (Fig. 11c), they used a biphasic liquid system, capable of generating microbubbles at a low optical power/temperature by formulating perfluoropentane (C_5F_{12} , PFP) as a volatile, water-immiscible component in the aqueous medium. The plasmonic Au substrate was functionalized with the capture protein, and the solution contained a low concentration of the target protein (Fig. 11d). The Marangoni flow around the PFP vapor bubble concentrated the analyte protein near the bubble, accelerating the protein binding. They observed the surface binding was enhanced by 1 order of magnitude within 1 min in the presence of bubbles, compared to that from static incubation for 30 min. This bubble-based method is exciting because it offers a simple yet effective way toward improving the performances of convective surface-based assay platforms.

5 Conclusions

In conclusion, motivated by the easy accessibility and multifunctionality of gas bubbles, analytical chemists have recently developed many new bubble-based analytical strategies. These strategies were built upon different characteristic properties of gas bubbles, including the gas/liquid interfacial activity, acoustic resonance, electrical insulation and discharge, deformability, and unique mass transport behaviors. Their applications range from surface-active compound detection and preconcentration to ultrasound imaging, acoustic detection,

single cell and organism manipulation and analysis, metal and gas sensing, and biosensing. Although the scope of this review did not include advancements in fundamental studies of gas bubble behaviors, such studies are essential for progress in this field. For example, the bubble-nucleation-based method for surfactant detection stems from the basic research on the gas bubble nucleation. The development of bubble film nanochannel biosensors was enabled by the fundamental knowledge of the electrokinetic properties of soap bubble nanofilms. Looking ahead, the recent increasing interest in understanding the bubble behaviors at the nanoscale^{9, 36, 133-140} and the new developments of bubble manipulation methods^{69, 141-146} will inspire new ideas and experimental attempts, lead to new findings regarding gas bubble properties that can be utilized for analytical applications, and therefore spur another wave of development of bubble-based analytical methods.

Conflicts of interest

There are no conflicts to declare.

Acknowledgments

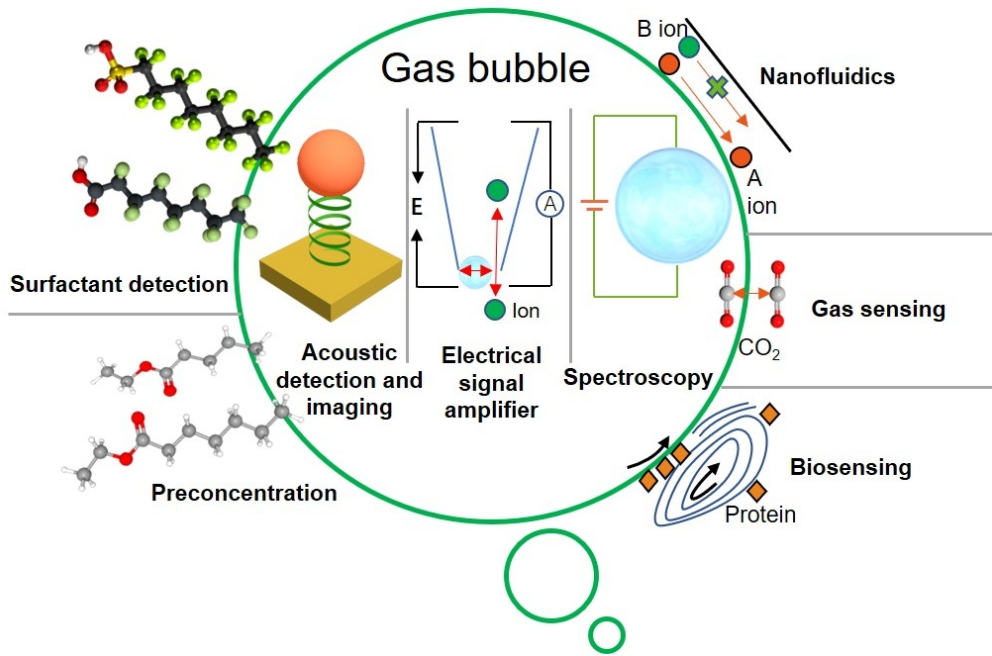
R. R., and L. L. gratefully acknowledge support from Chemical Measurement & Imaging Program, National Science Foundation (Award # CHE-1943737), the start-up funds and Competitive Graduate Research Assistantship (CGRA) Award from Wayne State University. S. A. gratefully acknowledge support from China Scholarship Council (CSC, grant number 201908410072).

References

1. Y. A. Perez Sirkin, E. D. Gadea, D. A. Scherlis and V. Molinero, *J. Am. Chem. Soc.*, 2019, **141**, 10801-10811.
2. X. Zhao, H. Ren and L. Luo, *Langmuir*, 2019, **35**, 5392-5408.
3. F. A. Garces-Pineda, M. Blasco-Ahicart, D. Nieto-Castro, N. Lopez and J. R. Galan-Mascaros, *Nat. Energy*, 2019, **4**, 519-525.
4. D. V. Esposito, *Joule*, 2017, **1**, 651-658.
5. W. Xu, Z. Lu, X. Sun, L. Jiang and X. Duan, *Acc. Chem. Res.*, 2018, **51**, 1590-1598.
6. Y. Feng, M. P. Schwarz, W. Yang and M. Cooksey, *Metall. Mater. Trans. B*, 2015, **46**, 1959-1981.
7. A. L. Perron, L. I. Kiss and S. Poncsák, *J. Appl. Electrochem.*, 2007, **37**, 303-310.
8. A. M. Soto, S. R. German, H. Ren, D. van der Meer, D. Lohse, M. A. Edwards and H. S. White, *Langmuir*, 2018, **34**, 7309-7318.
9. J. Chen, K. Zhou, Y. Wang, J. Gao, T. Yuan, J. Pang, S. Tang, H. Y. Chen and W. Wang, *Proc. Natl. Acad. Sci. U. S. A.*, 2019, **116**, 12678-12683.
10. S. Pradhan, R. J. Qader, B. R. Sedai and P. K. Bikina, *Sep. Purif. Technol.*, 2019, **217**, 31-39.
11. Y. Wang, M. E. Zaytsev, G. Lajoinie, H. L. The, J. C. T. Eijkel, A. van den Berg, M. Versluis, B. M. Weckhuysen, X. Zhang, H. J. W. Zandvliet and D. Lohse, *Proc. Natl. Acad. Sci. U. S. A.*, 2018, **115**, 7676-7681.
12. P. van der Linde, A. Moreno Soto, P. Penas-Lopez, J. Rodriguez-Rodriguez, D. Lohse, H. Gardeniers, D. van der Meer and D. Fernandez Rivas, *Langmuir*, 2017, **33**, 12873-12886.
13. D. Shin, J. B. Park, Y. J. Kim, S. J. Kim, J. H. Kang, B. Lee, S. P. Cho, B. H. Hong and K. S. Novoselov, *Nat. Commun.*, 2015, **6**, 6068.
14. X. Zhu, R. Verzicco, X. Zhang and D. Lohse, *Soft Matter*, 2018, **14**, 2006-2014.
15. C. M. Phan, A. V. Nguyen, J. D. Miller, G. M. Evans and G. J. Jameson, *Int. J. Miner. Process.*, 2003, **72**, 239-254.
16. J. Ralston, D. Fornasiero and R. Hayes, *Int. J. Miner. Process.*, 1999, **56**, 133-164.
17. Y. Shen, L. Hu, W. Chen, H. Xie and X. Fu, *Phys. Rev. Lett.*, 2018, **120**, 054503.
18. H. Chakibi, I. Hénaut, A. Salonen, D. Langevin and J. F. Argiller, *Energy Fuels*, 2018, **32**, 4049-4056.
19. R. F. Tabor, D. Y. Chan, F. Grieser and R. R. Dagastine, *Angew. Chem. Int. Ed.*, 2011, **50**, 3454-3456.
20. Á. Moreno Soto, T. Maddalena, A. Fraters, D. van der Meer and D. Lohse, *J. Fluid Mech.*, 2018, **846**, 143-165.
21. P. Lv, H. Le The, J. Eijkel, A. Van den Berg, X. Zhang and D. Lohse, *J. Phys. Chem. C*, 2017, **121**, 20769-20776.
22. G. B. Darband, M. Aliofkhaezaei and S. Shanmugam, *Renew. Sust. Energ. Rev.*, 2019, **114**, 109300.
23. I. Chakraborty, B. Ray, G. Biswas, F. Durst, A. Sharma and P. S. Ghoshdastidar, *Phys. Fluids*, 2009, **21**, 062103.
24. L. Zhang and M. Shoji, *Chem. Eng. Sci.*, 2001, **56**, 5371-5381.
25. J. L. Song, Z. A. Liu, X. Y. Wang, H. Liu, Y. Lu, X. Deng, C. J. Carmalt and I. P. Parkin, *J. Mater. Chem. A*, 2019, **7**, 13567-13576.
26. J. C. Bird, R. de Ruitter, L. Courbin and H. A. Stone, *Nature*, 2010, **465**, 759-762.
27. X. Wang, G. B. Deane, K. A. Moore, O. S. Ryder, M. D. Stokes, C. M. Beall, D. B. Collins, M. V. Santander, S. M. Burrows, C. M. Sultana and K. A. Prather, *Proc. Natl. Acad. Sci. U. S. A.*, 2017, **114**, 6978-6983.
28. C. F. Brasz, C. T. Bartlett, P. L. L. Walls, E. G. Flynn, Y. E. Yu and J. C. Bird, *Phys. Rev. Fluids*, 2018, **3**, 074001.
29. D. C. Blanchard, *Nature*, 1954, **173**, 1048-1048.
30. N. C. Christov, K. D. Danov, P. A. Kralchevsky, K. P. Anantha padmanabhan and A. Lips, *Langmuir*, 2006, **22**, 7528-7542.
31. P. Joos and E. Rillaerts, *J. Colloid Interface Sci.*, 1981, **79**, 96-100.
32. R. Ranaweera, C. Ghafari and L. Luo, *Anal. Chem.*, 2019, **91**, 7744-7748.
33. M. Blander and J. L. Katz, *AIChE J.*, 1975, **21**, 833-848.
34. P. G. Bowers, K. BarEli and R. M. Noyes, *J. Chem. Soc., Faraday Trans.*, 1996, **92**, 2843-2849.
35. L. Luo and H. S. White, *Langmuir*, 2013, **29**, 11169-11175.
36. R. Ranaweera and L. Luo, *Curr. Opin. Electrochem.*, 2020, **22**, 102-109.
37. Q. Chen, R. Ranaweera and L. Luo, *J. Phys. Chem. C*, 2018, **122**, 15421-15426.
38. Q. Chen and L. Luo, *Langmuir*, 2018, **34**, 4554-4559.
39. J. Y. Aller, M. R. Kuznetsova, C. J. Jahns and P. F. Kemp, *J. Aerosol Sci.*, 2005, **36**, 801-812.
40. C. J. McMurdo, D. A. Ellis, E. Webster, J. Butler, R. D. Christensen and L. K. Reid, *Environ. Sci. Technol.*, 2008, **42**, 3969-3974.
41. T. H. Bertram, R. E. Cochran, V. H. Grassian and E. A. Stone, *Chem. Soc. Rev.*, 2018, **47**, 2374-2400.
42. T. W. Wilson, L. A. Ladino, P. A. Alpert, M. N. Breckels, I. M. Brooks, J. Browse, S. M. Burrows, K. S. Carlsaw, J. A. Huffman, C. Judd, W. P. Kiltathau, R. H. Mason, G. McFiggans, L. A. Miller, J. J. Najera, E. Polishchuk, S. Rae, C. L. Schiller, M. Si, J. V. Temprado, T. F. Whale, J. P. Wong, O. Wurl, J. D. Yakobi-Hancock, J. P. Abbatt, J. Y. Aller, A. K. Bertram, D. A. Knopf and B. J. Murray, *Nature*, 2015, **525**, 234-238.

43. R. E. Cochran, T. Jayarathne, E. A. Stone and V. H. Grassian, *J. Phys. Chem. Lett.*, 2016, **7**, 1692-1696.
44. K. Chingin, Y. Cai, J. Liang and H. Chen, *Anal. Chem.*, 2016, **88**, 5033-5036.
45. K. Chingin, Y. F. Cai, V. Chagovets, A. Kononikhin, N. Starodubtseva, V. Frankevich and H. W. Chen, *Metabolomics*, 2016, **12**, 171.
46. K. Chingin, R. Yan, D. Zhong and H. Chen, *ACS Omega*, 2018, **3**, 8709-8717.
47. W. Kou, H. Zhang, C. Konstantin and H. W. Chen, *Chin. J. Anal. Chem.*, 2017, **45**, 1937-1942.
48. Y. Gao, B. Xia, Y. Qin, K. Huang, C. Yang, Q. Yang and L. Zhao, *J. Agric. Food Chem.*, 2020, **68**, 5732-5740.
49. Y. Cao, C. Lee, E. T. J. Davis, W. Si, F. Wang, S. Trimpin and L. Luo, *Anal. Chem.*, 2019, **91**, 14352-14358.
50. J. Magnaudet and I. Eames, *Annu. Rev. Fluid. Mech.*, 2000, **32**, 659-708.
51. A. Taqieddin, R. Nazari, L. Rajic and A. Alshawabkeh, *J. Electrochem. Soc.*, 2017, **164**, E448-E459.
52. A. Taqieddin, M. R. Allshouse and A. N. Alshawabkeh, *J. Electrochem. Soc.*, 2018, **165**, E694-E711.
53. C. H. Chang and P. L. Urban, *Anal. Chem.*, 2016, **88**, 8735-8740.
54. H. C. Yang and P. L. Urban, *Anal. Bioanal. Chem.*, 2019, **411**, 2511-2520.
55. H. C. Yang, C. M. Chang and P. L. Urban, *Heliyon*, 2019, **5**, e01639.
56. H. C. Yang, C. H. Chang and P. L. Urban, *J. Vis. Exp.*, 2017, e56008.
57. A. Sahu and P. Subramaniam, *Ind. Eng. Chem. Res.*, 2018, **57**, 11414-11423.
58. D. P. Elpa, S. P. Wu and P. L. Urban, *Anal. Chem.*, 2020, **92**, 2756-2763.
59. W. Lauterborn and T. Kurz, *Rep. Prog. Phys.*, 2010, **73**, 106501.
60. J. R. Lindner, *Nat. Rev. Drug. Discov.*, 2004, **3**, 527-532.
61. E. Quaia, *Contrast media in ultrasonography: basic principles and clinical applications*, Springer, 2006.
62. E. Quaia, *Eur. Radiol.*, 2007, **17**, 1995-2008.
63. D. Cosgrove, *Eur. J. Radiol.*, 2006, **60**, 324-330.
64. S. B. Feinstein, B. Coll, D. Staub, D. Adam, A. F. Schinkel, F. J. ten Cate and K. Thomenius, *J. Nucl. Cardiol.*, 2010, **17**, 106-115.
65. S. G. Zheng, H. X. Xu, L. N. Liu, M. D. Lu, X. Y. Xie, W. P. Wang, B. Hu, K. Yan, H. Ding, S. S. Tang, L. X. Qian and B. M. Luo, *Clin. Hemorheol. Microcirc.*, 2013, **55**, 359-374.
66. M. Claudon, D. Cosgrove, T. Albrecht, L. Bolondi, M. Bosio, F. Calliada, J. M. Correas, K. Darge, C. Dietrich, M. D'Onofrio, D. H. Evans, C. Filice, L. Greiner, K. Jager, N. Jong, E. Leen, R. Lencioni, D. Lindsell, A. Martegani, S. Meairs, C. Nolsoe, F. P. Piscaglia, P. Ricci, G. Seidel, B. Skjoldbye, L. Solbiati, L. Thorelius, F. Tranquart, H. P. Weskott and T. Whittingham, *Ultraschall Med.*, 2008, **29**, 28-44.
67. P. Koczera, L. Appold, Y. Shi, M. Liu, A. Dasgupta, V. Pathak, T. Ojha, S. Fokong, Z. Wu, M. van Zandvoort, O. Iranzo, A. J. C. Kuehne, A. Pich, F. Kiessling and T. Lammers, *J. Control Release*, 2017, **259**, 128-135.
68. K. R. Volz, K. D. Evans, C. D. Kanner, J. A. Buford, M. Freimer and C. M. Sommerich, *J. Diagn. Med. Sonogr.*, 2016, **33**, 102-111.
69. T. Segers, E. Gaud, G. Casqueiro, A. Lassus, M. Versluis and P. Frinking, *Appl. Phys. Lett.*, 2020, **116**, 173701.
70. M. Postema, A. Novell, C. Sennoga, A. T. Poortinga and A. Boenkaz, *Applied Acoustics*, 2018, **137**, 148-150.
71. A. Bretagne, A. Tourin and V. Leroy, *Appl. Phys. Lett.*, 2011, **99**, 221906.
72. M. Yang and P. Sheng, *Annu. Rev. Fluid Mech.*, 2017, **47**, 83-114.
73. E. Bok, J. J. Park, H. Choi, C. K. Han, O. B. Wright and S. H. Lee, *Phys. Rev. Lett.*, 2018, **120**, 044302.
74. T. Brunet, J. Leng and O. Mondain-Monval, *Science*, 2013, **342**, 323-324.
75. Z. R. Cai, S. D. Zhao, Z. D. Huang, Z. Li, M. Su, Z. Y. Zhang, Z. P. Zhao, X. T. Hu, Y. S. Wang and Y. L. Song, *Adv. Funct. Mater.*, 2019, **29**, 1906984.
76. Z. Huang, S. Zhao, M. Su, Q. Yang, Z. Li, Z. Cai, H. Zhao, X. Hu, H. Zhou, F. Li, J. Yang, Y. Wang and Y. Song, *ACS Appl. Mater. Interfaces*, 2020, **12**, 1757-1764.
77. G. M. Whitesides, *Nature*, 2006, **442**, 368-373.
78. S. L. Anna, *Annu. Rev. Fluid Mech.*, 2016, **48**, 285-309.
79. M. Hashimoto, S. S. Shevkoplyas, B. Zasonska, T. Szymborski, P. Garstecki and G. M. Whitesides, *Small*, 2008, **4**, 1795-1805.
80. A. Huerre, V. Miralles and M. C. Jullien, *Soft Matter*, 2014, **10**, 6888-6902.
81. A. Hashmi, G. Yu, M. Reilly-Collette, G. Heiman and J. Xu, *Lab Chip*, 2012, **12**, 4216-4227.
82. A. J. Conde, I. Keraite, A. E. Ongaro and M. Kersaudy-Kerhoas, *Lab Chip*, 2020, **20**, 741-748.
83. D. Ahmed, A. Ozcelik, N. Bojanala, N. Nama, A. Upadhyay, Y. Chen, W. Hanna-Rose and T. J. Huang, *Nat. Commun.*, 2016, **7**, 11085.
84. W. Cui, L. Mu, X. Duan, W. Pang and M. A. Reed, *Nanoscale*, 2019, **11**, 14625-14634.
85. S. Orbay, A. Ozcelik, J. Lata, M. Kaynak, M. Wu and T. J. Huang, *J. Micromech. Microeng.*, 2017, **27**, 015008.
86. Y. Xie, N. Nama, P. Li, Z. Mao, P. H. Huang, C. Zhao, F. Costanzo and T. J. Huang, *Small*, 2016, **12**, 902-910.
87. Y. L. Ying, Y. X. Hu, R. Gao, R. J. Yu, Z. Gu, L. P. Lee and Y. T. Long, *J. Am. Chem. Soc.*, 2018, **140**, 5385-5392.
88. Y. Yang, Y. I. Cho and A. Fridman, *Plasma discharge in liquid: water treatment and applications*, CRC press, 2017.
89. Y. Tu, H. Xia, Y. Yang and X. Lu, *Phys. Plasmas*, 2016, **23**, 013507.
90. C. Yamabe, F. Takeshita, T. Miichi, N. Hayashi and S. Ihara, *Plasma Processes Polym.*, 2005, **2**, 246-251.
91. Y. Kohara, Y. Terui, M. Ichikawa, K. Yamamoto, T. Shirasaki, K. Kohda, T. Yamamoto and Y. Takamura, *J. Anal. At. Spectrom.*, 2015, **30**, 2125-2128.
92. V. K. Do, M. Yamamoto, S. Taguchi, Y. Takamura, N. Surugaya and T. Kuno, *Talanta*, 2018, **183**, 283-289.
93. S. Barua, I. M. M. Rahman, M. Miyaguchi, A. S. Mashio, T. Maki and H. Hasegawa, *Sens. Actuators B: Chem.*, 2018, **272**, 91-99.
94. A. Hamdan and M. S. Cha, *J. Phys. D: Appl. Phys.*, 2016, **49**, 245203.
95. S. R. Liu and P. K. Dasgupta, *Anal. Chem.*, 1995, **67**, 2042-2049.
96. M. A. Jeannot and F. F. Cantwell, *Anal. Chem.*, 1996, **68**, 2236-2240.
97. D. B. Williams, M. J. George, R. Meyer and L. Marjanovic, *Anal. Chem.*, 2011, **83**, 6713-6716.
98. D. B. Williams, M. J. George and L. Marjanovic, *J. Agric. Food Chem.*, 2014, **62**, 7676-7681.
99. L. Guo, N. Binte Nawi and H. K. Lee, *Anal. Chem.*, 2016, **88**, 8409-8414.
100. C. A. T. H. M. Lee and H. K. Lee, *LC GC N. Am.*, 2019, **32**, 318-325.
101. K. Chullasat, Z. Z. Huang, O. Bunkoed, P. Kanatharana and H. K. Lee, *Microchem. J.*, 2020, **155**, 104666.
102. M. J. George, N. E. Madala and I. A. Dubery, *Int. J. Environ. Anal. Chem.*, 2019, **99**, 1198-1210.

103. M. J. George, L. Marjanovic and D. B. G. Williams, *Talanta*, 2015, **144**, 445-450.
104. P. S. Epstein and M. S. Plesset, *J. Chem. Phys.*, 1950, **18**, 1505-1509.
105. A. Bulbul and H. Kim, *Lab Chip*, 2015, **15**, 94-104.
106. A. Bulbul, S. B. Amar and K. Hanseup, presented in part at the Proc μ TAS, 2013.
107. A. Bulbul and H. Kim, 19th International Conference on Solid-State Sensors, Actuators and Microsystems (TRANSDUCERS), Kaohsiung, Taiwan, 2017.
108. A. Bulbul, K. Kim and H. Kim, 2019 IEEE 32nd International Conference on Micro Electro Mechanical Systems (MEMS), Seoul, Korea, 2019.
109. S. Seo, M. Mastiani, M. Hafez, G. Kunkel, C. G. Asfour, K. I. Garcia-Ocampo, N. Linares, C. Saldana, K. Yang and M. Kim, *Int. J. Greenh. Gas Control.*, 2019, **83**, 256-264.
110. S. Seo, M. Nguyen, M. Mastiani, G. Navarrete and M. Kim, *Anal. Chem.*, 2017, **89**, 10827-10833.
111. S. Seo, G. A. Perez, K. Tewari, X. Comas and M. Kim, *Sci Rep.*, 2018, **8**, 11786.
112. T. Kanyanee, W. L. Borst, J. Jakmunee, K. Grudpan, J. Li and P. K. Dasgupta, *Anal. Chem.*, 2006, **78**, 2786-2793.
113. T. Kanyanee, J. Jakmunee, K. Grudpan and P. K. Dasgupta, *J. Am. Chem. Soc.*, 2010, **132**, 18045-18047.
114. J. Fu and L. Zhang, *Anal. Chem.*, 2018, **90**, 8080-8085.
115. J. Fu and L. Zhang, *Anal. Chem.*, 2018, **90**, 1356-1362.
116. O. Bonhomme, O. Liot, A. L. Biance and L. Bocquet, *Phys. Rev. Lett.*, 2013, **110**, 054502.
117. O. Bonhomme, A. Mounier, G. Simon and A. L. Biance, *J. Phys. Condens. Matter.*, 2015, **27**, 194118.
118. L. Joly, F. Detcheverry and A. L. Biance, *Phys. Rev. Lett.*, 2014, **113**, 088301.
119. W.-J. Lan, M. A. Edwards, L. Luo, R. T. Perera, X. Wu, C. R. Martin and H. S. White, *Acc. Chem. Res.*, 2016, **49**, 2605-2613.
120. X. Hou, W. Guo and L. Jiang, *Chem. Soc. Rev.*, 2011, **40**, 2385-2401.
121. Y. Ma, M. Sun, X. Duan, A. van den Berg, J. C. T. Eijkel and Y. Xie, *Nat. Commun.*, 2020, **11**, 814.
122. S. J. Kim, S. H. Ko, K. H. Kang and J. Han, *Nat. Nanotechnol.*, 2010, **5**, 297-301.
123. M. Li and R. K. Anand, *Analyst*, 2016, **141**, 3496-3510.
124. X. Li, L. Luo and R. M. Crooks, *Anal. Chem.*, 2017, **89**, 4294-4300.
125. X. G. Yang, D. Baczymalski, C. Cierpka, G. Mutschke and K. Eckert, *Phys. Chem. Chem. Phys.*, 2018, **20**, 11542-11548.
126. Y. Kim, H. Ding and Y. Zheng, *Nano Lett.*, 2020, DOI: 10.1021/acs.nanolett.0c01969.
127. L. E. Scriven and C. V. Sternling, *Nature*, 1960, **187**, 186-188.
128. J. Massing, G. Mutschke, D. Baczymalski, S. S. Hossain, X. Yang, K. Eckert and C. Cierpka, *Electrochim. Acta*, 2019, **297**, 929-940.
129. K. Setoura, S. Ito and H. Miyasaka, *Nanoscale*, 2017, **9**, 719-730.
130. B. B. Rajeeva, M. A. Alabandi, L. Lin, E. P. Perillo, A. K. Dunn and Y. Zheng, *J. Mater. Chem. C*, 2017, **5**, 5693-5699.
131. L. Lin, X. Peng, Z. Mao, W. Li, M. N. Yogeesh, B. B. Rajeeva, E. P. Perillo, A. K. Dunn, D. Akinwande and Y. Zheng, *Nano Lett.*, 2016, **16**, 701-708.
132. A. Kotnala, P. S. Kollipara, J. Li and Y. Zheng, *Nano Lett.*, 2020, **20**, 768-779.
133. S. M. Lu, Y. J. Li, J. F. Zhang, Y. Wang, Y. L. Ying and Y. T. Long, *Anal. Chem.*, 2019, **91**, 10361-10365.
134. Y. Wang, J. Chen, Y. Jiang, X. Wang and W. Wang, *Anal. Chem.*, 2019, **91**, 4665-4671.
135. H. Ren, M. A. Edwards, Y. Wang and H. S. White, *J. Phys. Chem. Lett.*, 2020, **11**, 1291-1296.
136. Y. Wang, E. Gordon and H. Ren, *J. Phys. Chem. Lett.*, 2019, **10**, 3887-3892.
137. M. A. Edwards, H. S. White and H. Ren, *ACS Nano*, 2019, **13**, 6330-6340.
138. Q. Li, Y. L. Ying, S. C. Liu, Y. X. Hu and Y. T. Long, *Analyst*, 2020, **145**, 2510-2514.
139. Q. J. Chen, Y. W. Liu, M. A. Edwards, Y. L. Liu and H. S. White, *Anal. Chem.*, 2020, **92**, 6408-6414.
140. E. D. Gadea, Y. A. Perez Sirkin, V. Molinero and D. A. Scherlis, *J. Phys. Chem. Lett.*, 2020, DOI: 10.1021/acs.jpcclett.0c01404.
141. C. Pei, Y. Peng, Y. Zhang, D. Tian, K. Liu and L. Jiang, *ACS Nano*, 2018, **12**, 5489-5494.
142. C. Yu, P. Zhang, J. Wang and L. Jiang, *Adv. Mater.*, 2017, **29**, 1703053.
143. J. Zhang, P. Liu, B. Yi, Z. Wang, X. Huang, L. Jiang and X. Yao, *ACS Nano*, 2019, **13**, 10596-10602.
144. C. M. Yu, M. Y. Cao, Z. C. Dong, J. M. Wang, K. Li and L. Jiang, *Adv. Funct. Mater.*, 2016, **26**, 3236-3243.
145. X. Xiao, C. Zhang, H. Ma, Y. Zhang, G. Liu, M. Cao, C. Yu and L. Jiang, *ACS Nano*, 2019, **13**, 4083-4090.
146. C. M. Yu, X. B. Zhu, M. Y. Cao, C. L. Yu, K. Li and L. Jiang, *J. Mater. Chem. A*, 2016, **4**, 16865-16870.



171x110mm (150 x 150 DPI)